Geol. Mag. **148** (*4*), *2011, pp. 580–596. © Cambridge University Press 2011*
doi:10.1017/S0016756810001020

Metamorphism and diachronous cooling in a contractional orogen: the Strandja Massif, NW Turkey

G. SUNAL*‡†, M. SATIR*, B. A. NATAL'IN‡, G. TOPUZ§ & O. VONDERSCHMIDT*

*Universität Tübingen, Institut für Geowissenschaften, Wilhelmstrasse 56, D-72074 Tübingen, Germany
‡İstanbul Teknik Üniversitesi, Jeoloji Mühendisliği Bölümü, TR-34469 Maslak, Istanbul, Turkey
§İstanbul Teknik Üniversitesi, Avrasya Yerbilimleri Enstitüsü, TR-34469 Maslak, Istanbul, Turkey

(*Received* 24 November 2009; *accepted* 1 November 2010; *first published online* 19 January 2011)

Abstract – The southern part of the Strandja Massif, northern Thrace, Turkey, comprises a basement of various gneisses, micaschists and rare amphibolite, and a cover of metaconglomerate and metasandstone, separated from each other by a pre-metamorphic unconformity. Metamorphic grade decreases from the epidote–amphibolite facies in the south to the albite–epidote–amphibolite/greenschist-facies transition in the north. Estimated *P–T* conditions are 485–530 °C and 0.60–0.80 GPa in the epidote–amphibolite facies domain, and decrease towards the transitional domain between greenschist- and epidote–amphibolite facies. Rb–Sr muscovite ages range from 162.9 ± 1.6 Ma to 149.1 ± 2.1 Ma, and are significantly older (279–296 Ma) in the northernmost part of the study area. The Rb–Sr biotite ages decrease from 153.9 ± 1.5 Ma in the south to 134.4 ± 1.3 Ma in the north. These age values in conjunction with the attained temperatures suggest that the peak metamorphism occurred at around 160 Ma and cooling happened diachronously, and Rb–Sr muscovite ages were not reset during the metamorphism in the northernmost part. Structural features such as (i) consistent S-dipping foliation and SW to SE-plunging stretching lineation, (ii) top-to-the-N shear sense, and (iii) N-vergent ductile shear zones and brittle thrusts suggest a N-vergent compressional deformation coupled with exhumation. We tentatively ascribe this metamorphism and subsequent diachronous cooling to the northward propagation of a thrust slice. The compressional events in the Strandja Massif were most probably related to the coeval N-vergent subduction/collision system in the southerly lying Rhodope Massif.

Keywords: *P–T* estimates, Rb–Sr dating, metamorphism and diachronous cooling, compressional exhumation, Strandja Massif, Turkey.

1. Introduction

Trending WNW–ESE across the border between Turkey and Bulgaria, the Strandja Massif forms an approximately 300 km long and 100 km wide metamorphic belt. The Strandja Massif is bounded by the metamorphic rocks of the Rhodope Massif to the S and SW, and upper Cretaceous volcanics of the Sredna Gora zone to the N. Middle Mesozoic amphibolite–greenschist facies metamorphism and the presence of N-vergent compressional structures have long been known (Chatalov, 1991; Okay *et al*. 2001). Its metamorphic characteristics and age of deformation are, however, poorly known for both its basement and the cover units. Only few and sparsely distributed age data are available to the geological community (e.g. Okay *et al*. 2001). Metamorphic facies discriminated so far are rather coarse and made only on the basis of mineral paragenesis of the rocks, such as amphibolite–greenschist facies (Okay *et al*. 2001).

In this study we aim to determine the metamorphic conditions that occurred in the Strandja Massif in detail and the age of deformation and its meaning for the metamorphic history of the region. For petrological analyses, eight samples are studied in order to reveal the metamorphic evolution of the Strandja Massif. The Rb–Sr dating method is used on both biotites and white micas from 21 samples to determine the time of metamorphism and subsequent cooling. The time of cooling to specific temperatures can be determined using different minerals through different dating methods taking into account the closure temperature concept (blocking or isotopic closure temperature) (Dodson, 1973; Villa, 1998). The isotopic closure temperature may also be used to infer the age of exhumation or exhumation rate of a region. For this, isotopic closure temperatures of different minerals are converted to depths assuming a geothermal gradient. However, there are debates about both the closure temperature concept and converting temperature data to exhumation rates. Recent studies indicate that the isotopic closure temperature of a specific mineral can be a function of various processes such as solid-state diffusion parameters, effective grain size, temperature, cooling rate, fluid activity, deformation and surrounding exchange medium (Dodson, 1973; Villa, 1998; Montel, Kornprobst & Vielzeuf, 2000; Müller, Aerden & Halliday, 2000; Kühn *et al*. 2000; Glodny *et al*. 2003, 2005; Reddy *et al*. 2003; Glodny, Kühn & Austrheim, 2008). The metamorphic conditions of the Strandja Massif allow us to suggest that white mica Rb–Sr ages show the time of the deformation

†Author for correspondence: gsunal@itu.edu.tr

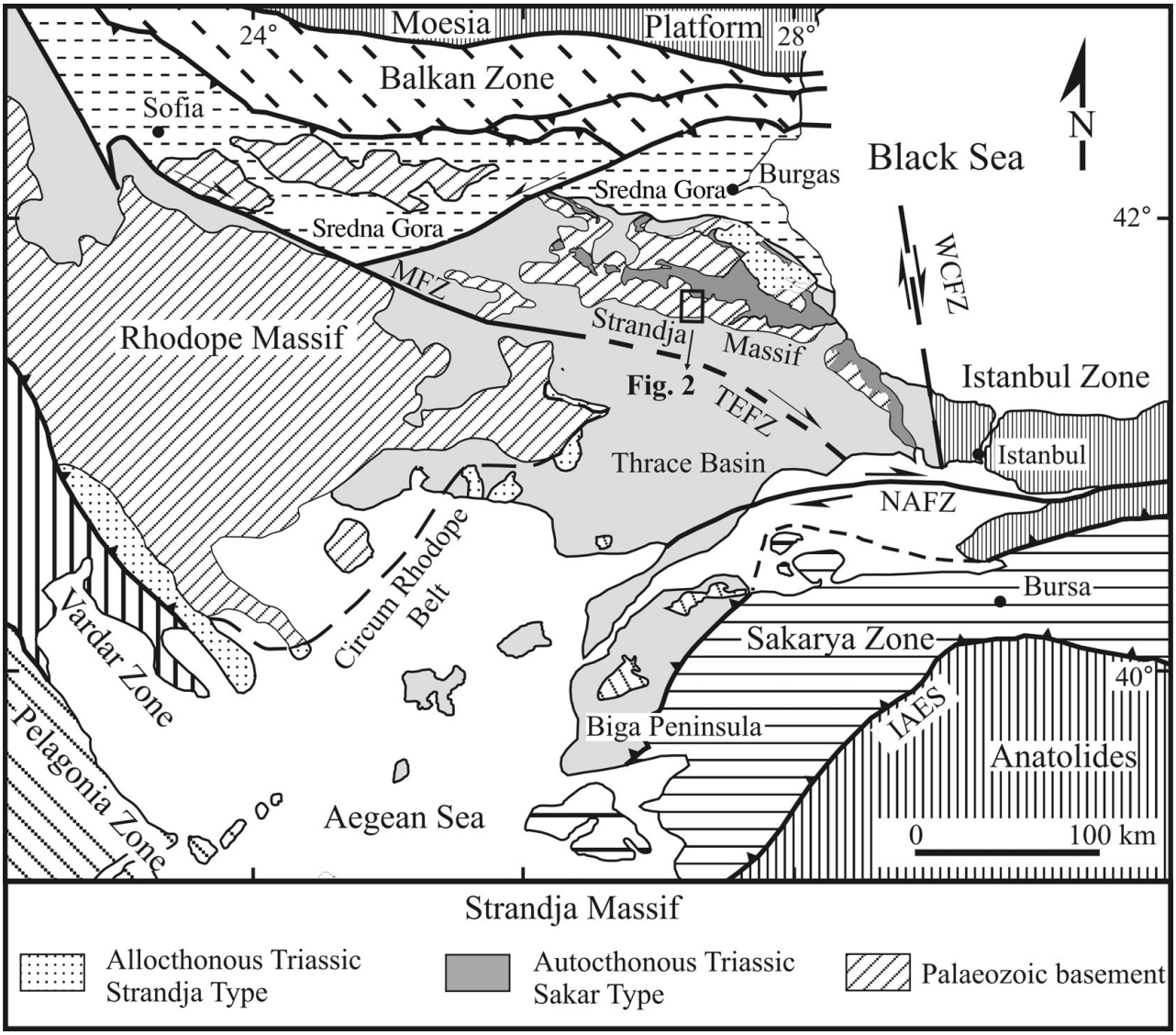

Figure 1. Main tectonic units of the northern Aegean, the Balkanides and NW Turkey (modified after Okay & Satır, 2000). IAES – Izmir-Ankara-Erzincan suture; NAFZ – North Anatolian Fault Zone; MFZ – Maritsa Fault Zone; WCFZ – West Crimean Fault. Coordinates are degrees (latitude N and longitude E).

during the epidote–amphibolite-facies conditions and biotite ages represent cooling through greenschist-facies conditions.

2. Geological setting and field relations

The Strandja Massif is unconformably overlain by either unmetamorphosed Upper Cretaceous volcanic and volcanoclastic rocks to the north or by an Eocene–Oligocene sequence of limestone, sandstone and shale to the south (Fig. 1). To date, three tectonostratigraphic units are differentiated in the Strandja Massif: (i) a Palaeozoic basement comprising micaschist and various types of orthogneiss and amphibolite (Okay *et al*. 2001; Natal'in *et al*. 2005; Natal'in, Sunal & Toraman, 2005; Sunal *et al*. 2006, 2008), (ii) a Lower to Middle Triassic to Middle Jurassic cover sequence (Chatalov 1991; E. Toraman, unpub. M.Sc. thesis, İstanbul Tech. Univ., 2002) consisting of metaconglomerate, metasandstone, phyllite, calc-phyllite and marble (Okay *et al*. 2001; Hagdorn & Göncüoğlu, 2007), and (iii) an allochthonous unit of Triassic metasedimentary and metavolcanic rocks, which was thrust onto the former two units (e.g. Chatalov, 1991; Gerdjikov, 2005).

The Strandja Massif underwent greenschist- to lower amphibolite-facies metamorphism during Late Jurassic time (Okay *et al*. 2001; Lilov, Maliakov & Balogh, 2004; Natal'in *et al*. 2005; Natal'in, Sunal & Toraman, 2005). Furthermore, the Palaeozoic basement rock association of the Strandja Massif was involved in a pre-Triassic (pre-Permian?) regional metamorphic event, which is deduced from (i) a discordance between the internal foliation of metagranite clasts and that of the matrix of the basal metaconglomerate of the cover sequence (E. Toraman, unpub. M.Sc. thesis, İstanbul Tech. Univ., 2002; Gerdjikov, 2005; Natal'in *et al*. 2005; Natal'in, Sunal & Toraman, 2005), (ii) the presence of two distinct foliations in pre-Permian orthogneisses (Natal'in *et al*. 2005; Natal'in, Sunal &

https://doi.org/10.1017/S0016756810001020 Published online by Cambridge University Press

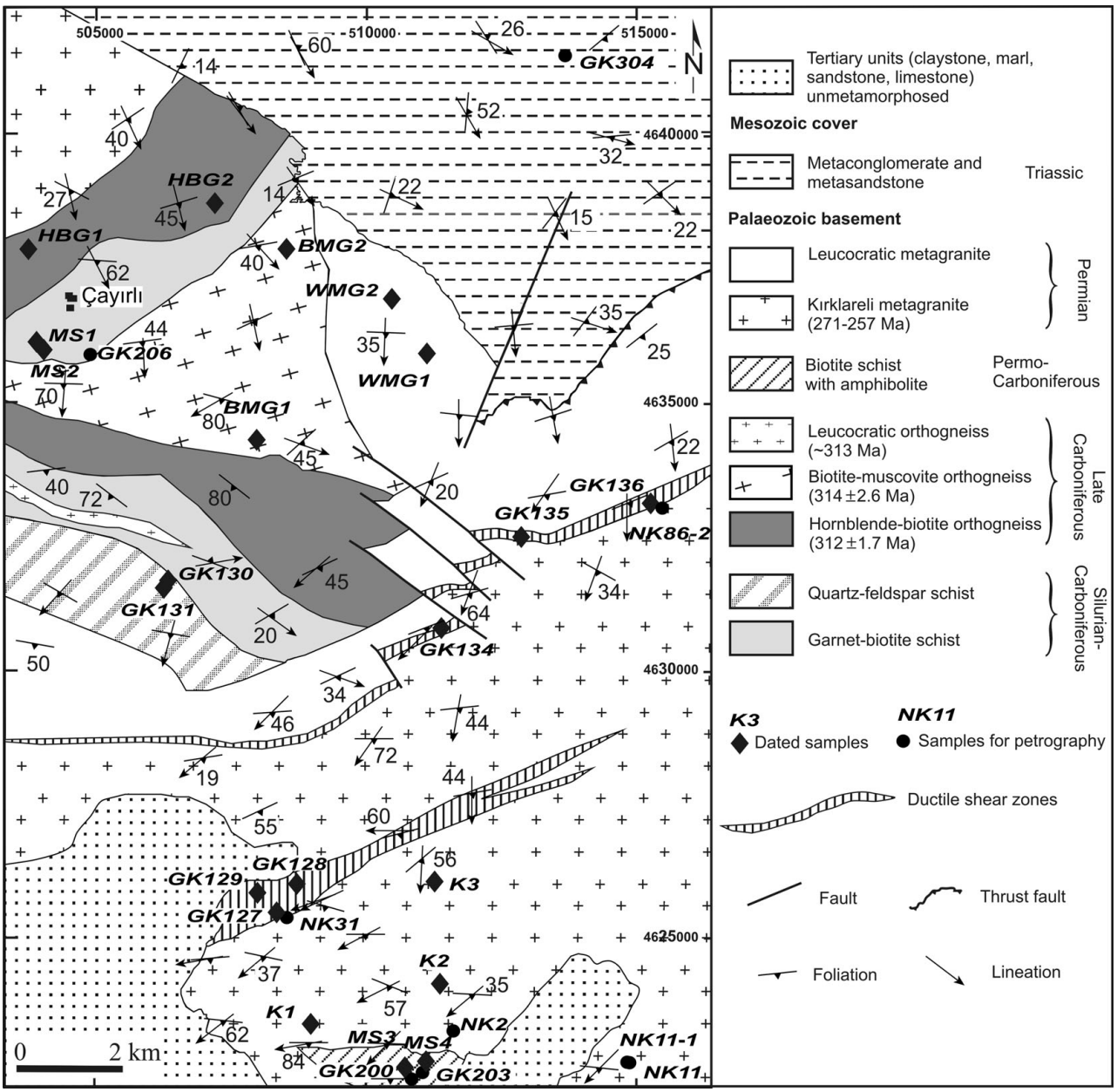

Figure 2. Geological map of the study area. For location see Figure 1 (coordinates are UTM, European (ED50) and Zone 35).

Toraman, 2005), and (iii) the presence of a migmatitic gneiss with a Pb–Pb zircon evaporation age of 285 ± 13 Ma (Okay *et al*. 2001). The metamorphic grade of the older pre-Triassic (pre-Permian?) metamorphism is not constrained.

We studied a 15 km by 20 km area on the southern margin of the Strandja Massif where the pre-Triassic basement and the Triassic cover sequence are exposed (Figs 1, 2). The pre-Triassic basement is represented by various types of strongly- to weakly-foliated metagranites, orthogneisses, micaschists and amphibolites, while the Triassic cover sequence consists of a metasedimentary series starting with metaconglomerates and passing into metasandstones.

The metagranites and orthogneisses comprise the Kırklareli metagranite, leucocratic metagranite, hornblende–biotite orthogneiss and biotite–muscovite orthogneiss. Intrusive contacts and up to 2 m thick mafic microgranular enclaves are still recognizable in the Kırklareli metagranite and hornblende–biotite orthogneiss. The Kırklareli metagranite is pinkish grey and displays an augen gneiss structure defined by K-feldspar and locally plagioclase porphyroclasts in a relatively fine-grained matrix. The leucocratic metagranite differs from the Kırklareli metagranite in its leucocratic and fine-grained nature. The hornblende–biotite orthogneiss is greenish dark grey and has an equigranular texture. The biotite–muscovite orthogneiss has a fine-grained equigranular texture. The leucocratic metagranite occurs as 0.5 to 25 m thick dykes in the hornblende–biotite, biotite–muscovite and biotite schists. The Pb–Pb evaporation ages of igneous zircons crystallized in the magmatic precursors of these orthogneisses yielded ages ranging from 315 to 256 Ma, testifying to the presence of the Late Carboniferous to Permian magmatic activity in the

https://doi.org/10.1017/S0016756810001020 Published online by Cambridge University Press

Table 1. Selected representative analyses of epidote minerals from basement amphibolites, orthogneisses and schists

	Basement gneisses				Basement amphibolites				Basement schists			
	NK11		**NK86-2**		**NK 11-1**		**GK203**		**GK200**		**GK206**	
SiO_2	37.74	37.77	38.08	37.66	38.53	38.08	36.02	35.44	38.09	37.94	37.17	38.29
TiO_2	0.15	0.08	0.10	0.12	0.12	0.10	0.06	0.09	0.12	0.27	0.20	0.25
Al_2O_3	25.16	25.02	24.69	24.03	26.35	25.38	23.65	22.91	26.31	27.47	24.16	26.59
Cr_2O_3	0.02	0.00	0.00	0.00	0.01	0.00	0.03	0.00	0.09	0.03	0.09	0.05
FeO	10.77	10.29	10.33	11.42	8.81	10.72	9.90	10.23	9.04	7.63	9.98	7.88
MnO	0.41	0.34	0.37	0.42	0.31	0.30	0.26	0.17	0.31	0.19	0.21	0.26
MgO	0.04	0.03	0.00	0.00	0.08	0.00	0.27	0.43	0.03	0.09	0.01	0.01
CaO	22.72	23.19	22.68	22.73	23.23	22.57	20.26	19.39	23.48	23.29	22.36	23.14
Na_2O	0.02	0.00	0.00	0.00	0.00	0.00	0.03	0.03	0.01	0.03	0.01	0.04
K_2O	0.00	0.00	0.02	0.03	0.00	0.05	0.00	0.02	0.02	0.00	0.00	0.02
Total	97.03	96.70	96.25	96.41	97.44	97.20	90.48	88.69	97.49	96.92	94.18	96.52
Cation occupation on the basis of 12.5 oxygens.												
Si	2.976	2.989	3.022	2.998	3.007	2.992	2.992	2.986	2.980	2.969	3.035	3.011
Ti	0.009	0.005	0.006	0.007	0.007	0.006	0.003	0.018	0.007	0.016	0.007	0.014
Al	2.339	2.333	2.309	2.254	2.424	2.350	2.264	2.207	2.425	2.533	2.314	2.464
Cr	0.001	0.000	0.000	0.000	0.001	0.000	0.001	0.003	0.005	0.002	0.007	0.003
Fe^{3+}	0.711	0.681	0.685	0.760	0.575	0.704	0.756	0.799	0.591	0.499	0.648	0.518
Mn	0.028	0.023	0.025	0.028	0.020	0.020	0.009	0.004	0.020	0.012	0.033	0.017
Mg	0.005	0.004	0.000	0.000	0.009	0.000	0.002	0.003	0.003	0.010	0.000	0.002
Ca	1.920	1.966	1.928	1.939	1.943	1.900	1.964	1.971	1.968	1.953	1.928	1.949
Na	0.004	0.000	0.000	0.000	0.000	0.000	1.000	1.000	0.002	0.004	0.001	0.005
K	0.000	0.000	0.002	0.003	0.000	0.005	0.000	0.000	0.002	0.000	0.003	0.002
Total	7.991	8.000	7.977	7.989	7.986	7.977	7.994	7.993	8.004	7.999	7.976	7.986
X_{Fe}	0.23	0.23	0.23	0.25	0.19	0.23	0.25	0.27	0.20	0.16	0.22	0.17

X_{Fe} – Fe/(Fe+Al); total Fe has been assumed to be Fe^{3+}.

Strandja Massif (Okay *et al*. 2001; Natal'in *et al*. 2005; Natal'in, Sunal & Toraman, 2005; Sunal *et al*. 2006).

The micaschists are of two types: Type-1 is represented by garnet–biotite schists, type-2 by biotite schists. Type-1 micaschists are exposed in the middle part of the study area and are of sedimentary origin as testified by detrital zircons with Pb–Pb evaporation ages of 460 to 2700 Ma (Sunal *et al*. 2008). Type-2 is associated with the well-foliated amphibolites and exposed in the southernmost part of the study area (Fig. 2).

The metaconglomerate of the cover sequence comprises stretched and elongated gravels (aspect ratio ranges between 1:2 and 1:4) of orthogneiss and quartzite, ranging from 1 to 30 cm in size in a well-foliated matrix. Some orthogneiss clasts in the metaconglomerate, originating from the basement units, contain an old foliation which is discordant to the matrix foliation, suggesting derivation from a pre-Triassic metamorphic domain (E. Toraman, unpub. M.Sc. thesis, İstanbul Tech. Univ., 2002; Gerdjikov, 2005; Natal'in *et al*. 2005; Natal'in, Sunal & Toraman, 2005). The metasandstones are characterized by a fine grain size (Ø ∼ 1 mm) and a greenish colour. Bedding and cross-bedding are locally recognizable.

The foliation generally strikes in an E–W direction, dipping at 20–60° to the south, and commonly crosscuts the lithological boundaries (Fig. 2) (Natal'in *et al*. 2005). However, local bending of the foliation occurs owing to folding. The stretching lineation plunges on average to the south at 10 to 60°. The orthogneisses are dissected by two mylonite zones: one is approximately 400 m thick and 5 km long, and is represented by biotite mylonites in the Kırklareli metagranite (Fig. 2); the second is represented by a ∼ 100 m thick and ∼ 15 km long muscovite mylonite and defines the northern lithological boundary of the Kırklareli metagranite (Fig. 2; Natal'in *et al*. 2005).

Kinematic criteria such as oblique foliation, local mantled porphyroclasts and (S-C) structures consistently indicate a top-to-the-N sense of shear. Moreover, east of the study area, a large thrust slice consisting of basement orthogneisses was mapped lying along a shear zone with N–S lineation over the Triassic cover rocks (Okay *et al*. 2001; Natal'in *et al*. 2005; Natal'in, Sunal & Toraman, 2005), which indicates that the shear zone in the region studied is also of a contractional nature. N-vergent deformation has also been described from the other parts of the Strandja Massif (Çağlayan, Şengün & Yurtsever, 1988; Okay *et al*. 2001; Gerdjikov, 2005).

3. Petrography and mineral compositions

Over 100 thin-sections were petrographically examined, and nine of them were chosen for electron microprobe work. Estimated modal abundances of these nine samples are summarized in Table A1 (online Appendix at http://journals.cambridge.org/geo) and mineral compositions are listed in Tables 1–4 and shown in Figures 3, 4. Mineral analyses were performed at Heidelberg University using a CAMECA SX-51 microprobe equipped with five wavelength-dispersive spectrometers and an additional Si-Li detector (Oxford Instruments). Operating conditions were 15 kV accelerating voltage and 20 nA beam current. Counting times were usually 10 s except for Mg, Ca, Al (20 s) and Ti (30 s) in ilmenite. Beam

https://doi.org/10.1017/S0016756810001020 Published online by Cambridge University Press

Table 2. Selected representative analyses of a garnet grain from biotite schist GK206 (data from garnet grain shown in Fig. 6)

Area	oro	coo	ıro	orc	coc	orc	ıro	coo	oro
SiO_2	36.93	37.23	37.43	36.85	36.81	36.87	37.11	37.33	39.62
TiO_2	0.03	0.02	0.00	0.00	0.04	0.03	0.07	0.07	0.00
Al_2O_3	20.70	20.85	20.67	20.73	20.86	20.84	20.75	20.85	21.50
Cr_2O_3	0.01	0.00	0.00	0.00	0.00	0.00	0.00	0.00	0.00
FeO	26.32	27.28	25.84	30.60	32.35	30.70	25.27	26.45	23.76
MnO	9.55	7.62	7.17	7.69	6.95	7.95	7.08	7.46	9.13
MgO	1.78	1.93	1.80	2.42	2.55	2.34	1.66	2.00	1.31
CaO	4.19	4.87	6.90	1.60	1.21	1.33	8.01	5.77	4.23
Na_2O	0.01	0.06	0.03	0.01	0.03	0.02	0.01	0.05	1.11
K_2O	0.02	0.01	0.01	0.00	0.00	0.01	0.00	0.02	0.08
Total	99.53	99.87	99.84	99.89	100.79	100.08	99.96	100.00	100.73
Cation occupation on the basis of 12 oxygens									
Si	3.067	2.999	3.011	2.992	2.972	2.990	2.985	3.000	3.119
Ti	0.000	0.002	0.000	0.000	0.002	0.002	0.004	0.004	0.000
Al	1.919	1.981	1.959	1.984	1.985	1.992	1.967	1.975	1.995
Fe^{2+}	1.683	1.787	1.738	2.078	2.184	2.082	1.700	1.778	1.564
Mn	0.747	0.657	0.488	0.529	0.475	0.546	0.482	0.508	0.609
Mg	0.131	0.000	0.216	0.292	0.307	0.283	0.199	0.239	0.153
Ca	0.349	0.216	0.595	0.139	0.105	0.116	0.690	0.497	0.357
Na	0.152	0.364	0.004	0.001	0.005	0.003	0.002	0.008	0.169
K	0.004	0.001	0.001	0.000	0.000	0.001	0.000	0.002	0.008
Total	8.051	0.002	8.012	8.016	8.036	8.014	8.028	8.013	7.972
X_{Alm}	0.58	0.61	0.57	0.68	0.71	0.69	0.55	0.60	0.58
X_{Pyp}	0.05	0.08	0.07	0.10	0.10	0.09	0.06	0.08	0.06
X_{Grs}	0.12	0.14	0.20	0.05	0.03	0.04	0.22	0.14	0.13
X_{Sps}	0.26	0.17	0.16	0.17	0.15	0.18	0.16	0.18	0.23
Fe/Fe+Mg	0.93	0.89	0.89	0.88	0.88	0.88	0.90	0.88	0.91

oro – outer rim of overgrowth; coo – centre of overgrowth; ıro – inner rim of overgrowth orc – outer rim of the core; coc – centre of the core.

Table 3. Selected representative analyses of biotite and white micas from basement amphibolites, orthogneisses, schists and cover schists

	Basement orthogneisses						Basement amphibolites			Basement schists			Cover schist		
	NK86-2		**NK31**		**NK2**		**NK11**	**NK11-1**	**GK203**	**GK200**	**GK206**		**GK304**		
	Bt	Ms	Bt	Ms	Bt	Ms	Bt	Bt	Bt	Bt	Bt	Ms	Bt	Ms	Ms
SiO_2	35.78	47.29	36.39	46.62	35.11	48.20	36.56	36.56	36.73	36.74	36.28	46.59	38.94	49.21	46.09
TiO_2	2.20	1.21	1.71	0.14	2.39	0.08	1.88	1.99	2.31	1.23	1.54	0.40	1.29	0.51	0.68
Al_2O_3	15.76	29.62	15.83	28.48	16.04	28.04	16.60	16.16	15.99	16.54	17.42	32.52	14.23	25.21	32.28
Cr_2O_3	0.02	0.05	0.01	0.00	0.02	0.00	0.00	0.00	0.01	0.04	0.06	0.00	0.05	0.04	0.00
FeO	22.02	5.36	19.86	5.73	23.64	5.94	17.74	18.71	19.06	17.01	18.46	2.69	11.55	6.48	4.28
MnO	0.62	0.05	0.29	0.04	0.51	0.00	0.42	0.25	0.37	0.12	0.14	0.00	0.20	0.10	0.03
MgO	8.76	1.57	10.69	2.22	8.07	1.91	11.69	11.99	11.12	12.67	11.36	1.42	17.46	3.18	1.23
CaO	0.05	0.00	0.02	0.00	0.03	0.01	0.01	0.03	0.01	0.03	0.08	0.01	0.00	0.00	0.01
Na_2O	0.08	0.28	0.06	0.15	0.08	0.11	0.08	0.18	0.14	0.11	0.19	0.57	0.07	0.12	0.29
K_2O	9.04	10.06	9.52	10.91	8.60	10.70	9.62	9.05	9.45	9.07	8.87	10.36	10.06	10.32	10.37
Total	94.32	95.48	94.37	94.29	94.47	94.98	94.60	94.91	95.20	93.56	94.38	94.55	93.85	95.17	95.26
Cation occupation on the basis of 11 oxygens															
Si	2.799	3.204	2.813	3.225	2.759	3.296	2.790	2.785	2.802	2.811	2.768	3.148	2.907	3.368	3.117
Ti	0.129	0.061	0.099	0.007	0.141	0.004	0.108	0.114	0.132	0.071	0.088	0.020	0.072	0.026	0.035
Al	1.453	2.365	1.442	2.322	1.485	2.260	1.493	1.451	1.437	1.492	1.567	2.589	1.252	2.033	2.574
Cr	0.001	0.003	0.000	0.000	0.001	0.000	0.000	0.000	0.000	0.003	0.004	0.000	0.003	0.002	0.000
Fe^{2+}	1.440	0.304	1.284	0.331	1.553	0.339	1.132	1.192	1.216	1.088	1.178	0.152	0.721	0.371	0.242
Mn	0.041	0.003	0.019	0.003	0.034	0.000	0.027	0.016	0.024	0.008	0.009	0.000	0.013	0.006	0.002
Mg	1.021	0.158	1.232	0.229	0.945	0.195	1.330	1.362	1.264	1.445	1.292	0.143	1.943	0.324	0.124
Ca	0.004	0.000	0.001	0.000	0.002	0.001	0.001	0.002	0.001	0.002	0.006	0.001	0.000	0.000	0.001
Na	0.012	0.037	0.009	0.020	0.011	0.014	0.012	0.027	0.021	0.016	0.028	0.075	0.010	0.016	0.038
K	0.902	0.869	0.939	0.963	0.862	0.934	0.936	0.880	0.919	0.885	0.863	0.893	0.958	0.901	0.895
Total	7.802	7.004	7.840	7.099	7.794	7.043	7.830	7.829	7.817	7.821	7.804	7.021	7.877	7.047	7.027
X_{Mg}	0.41	0.34	0.49	0.41	0.38	0.36	0.54	0.53	0.51	0.57	0.52	0.48	0.73	0.47	0.34

X_{Mg} – $Mg/(Mg+Fe^{2+})$; all Fe has been assumed to be Fe^{2+}; Bt – biotite; Ms – muscovite/phengite.

diameter was usually ~ 1 μm except for feldspar analyses which were performed with a defocused beam (5–10 μm). Raw data were corrected for matrix effects with the help of the PAP algorithm (Pouchou & Pichoir, 1984, 1985) implemented by CAMECA. Synthetic and natural standards were used for calibration before each measurement session. Detection limits are generally in the order of 0.1 wt % of the element under consideration.

The Kırklareli metagranite consists of muscovite, biotite, microperthitic microcline, plagioclase, quartz and accessory epidote, zircon, apatite, titanite and magnetite. Foliation is defined by the parallel elongation of biotite and muscovite. Both microperthitic microcline

https://doi.org/10.1017/S0016756810001020 Published online by Cambridge University Press

Table 4. Selected representative analyses of amphiboles from amphibolites

Sample	GK203				NK11-1			
Area	core	rim	core	rim	core	rim	core	rim
SiO_2	43.56	41.96	43.08	42.71	43.54	41.56	42.59	41.47
TiO_2	0.52	0.56	0.56	0.54	1.32	0.56	0.87	0.39
Al_2O_3	12.87	14.21	12.99	13.55	11.47	13.28	11.88	13.25
Cr_2O_3	0.05	0.03	0.03	0.01	0.00	0.01	0.05	0.04
FeO	15.97	16.44	15.77	15.62	17.90	18.85	18.22	19.25
MnO	0.38	0.32	0.37	0.26	0.52	0.52	0.55	0.47
MgO	10.71	9.95	10.75	10.24	9.71	8.57	9.24	8.34
CaO	11.38	11.18	11.41	11.18	11.46	11.38	11.37	11.49
Na_2O	1.52	1.72	1.44	1.51	1.29	1.45	1.32	1.45
K_2O	0.35	0.45	0.41	0.41	0.64	0.66	0.92	0.67
Total	97.31	96.81	96.81	96.03	97.84	96.84	97.00	96.82
Cation occupation on the basis of 23 oxygens								
Si	6.424	6.248	6.381	6.383	6.477	6.274	6.420	6.275
$Al^{(IV)}$	1.576	1.752	1.619	1.617	1.523	1.726	1.580	1.725
$Al^{(VI)}$	0.660	0.740	0.650	0.770	0.489	0.636	0.530	0.638
Ti	0.058	0.062	0.062	0.060	0.147	0.063	0.099	0.044
Fe^{+3}	0.508	0.534	0.553	0.433	0.432	0.581	0.460	0.584
Cr	0.006	0.003	0.004	0.001	0.000	0.002	0.005	0.005
Mg	2.354	2.208	2.374	2.282	2.152	1.928	2.075	1.881
Fe^{+2}(C)	1.415	1.452	1.358	1.454	1.779	1.790	1.831	1.847
Mn(C)	0.000	0.000	0.000	0.000	0.000	0.000	0.000	0.000
Mg	0.000	0.000	0.000	0.000	0.000	0.000	0.000	0.000
Fe^{+2}(B)	0.047	0.061	0.043	0.066	0.016	0.008	0.006	0.004
Mn(B)	0.048	0.041	0.046	0.033	0.065	0.066	0.071	0.060
Ca	1.799	1.784	1.810	1.790	1.826	1.841	1.836	1.863
Na(B)	0.107	0.115	0.101	0.111	0.093	0.085	0.087	0.073
Na(A)	0.328	0.381	0.313	0.325	0.278	0.338	0.299	0.353
K	0.065	0.085	0.077	0.079	0.121	0.128	0.177	0.128
Total A	0.393	0.466	0.390	0.404	0.399	0.466	0.475	0.482
X_{Mg}	0.62	0.59	0.63	0.60	0.55	0.52	0.53	0.50

A, B and C stand for crystallographic sites in standard amphibole formula '$A_{0-1}B_2C_5T_8O_{22}(OH)_2$'; $Al^{(IV)}$ and $Al^{(VI)}$ refer to tetrahedral and octahedral aluminium, respectively. Calculation method by Schumacher (1997).

(X_{Or} ~ 0.94–0.98) and plagioclase (An_{2-34}) locally form porphyroclasts, representing mostly igneous relics (Figs 3a, 5c, d). Myrmekites are common. Muscovites display Si contents of 2.79–3.30 cations per 11 oxygens (Fig. 3c; Table 3). X_{Mg} values of biotites show a large scatter from 0.35 to 0.58 (Fig. 3b; Table 3). Epidotes are characterized by $Fe^{3+}/(Fe^{3+}+Al)$ of 0.18–0.27 (Fig. 3d; Table 1).

Amphibolites are usually well-foliated, and comprise hornblende, biotite (X_{Mg} ~ 0.49–0.57), plagioclase (An_{23-34}), chlorite (X_{Mg} ~ 0.55–0.62), epidote and variable amounts of quartz. Some of the plagioclase grains contain relic cores with An_{13-14}, coinciding with the peristerite gap. In addition some grains are reversely zoned. With an increase in the amount of quartz, amphibolites grade into amphibole-bearing biotite gneisses. Rutile, apatite, titanite and ilmenite form accessory phases. Epidote occurs both as inclusions in hornblende and as discrete grains in the matrix, and displays $X_{Fe^{3+}}$ values of 0.19–0.27 (Fig. 3d; Table 1). Generally the cores of the epidotes display lower $X_{Fe^{3+}}$ values relative to the rims. Hornblendes are characterized by tschermakitic compositions with X_{Mg} of 0.48–0.65 (Fig. 4; Table 4) and are compositionally zoned (Fig. 5a), whereby Si, Mg and Ca decrease, and Al, Fe and Na increase towards the rim (Table 4).

Garnet–biotite schists (Type-1) include biotite, plagioclase (An_{21-29}), epidote, quartz, garnet and accessory zircon, ilmenite and apatite. Garnet occurs as small sub- to idioblastic grains with very few or no inclusions (50–300 μm; Fig. 5b). They show a compositional range $Alm_{57-74}Pyp_{6-11}Grs_{22-3}Sps_{24-12}$ (Table 2). Each garnet grain consists of two domains, a core and an overgrowth, separated from each other by a compositional jump (Fig. 6). The core domains are characterized by Mg–Fe-richer and Ca-poorer compositions relative to the rims. Mn in both domains (core and overgrowth) increases rimwards. This compositional feature is characteristic of diffusion-controlled zoning (Spear, 2004). In this study, increased Mn content at the rim is interpreted as the result of diffusion resulting from retrograde metamorphism. Similar compositional jumps in garnets were ascribed either to polymetamorphism (e.g. Jeřábek *et al*. 2008) or fractionation and different garnet-forming reactions during a single metamorphic cycle (e.g. Konrad-Schmolke *et al*. 2008). Both garnet domains are inclusion-free, hindering any inference on the associated mineral phases during the growth of each garnet domain. Epidote is characterized by $X_{Fe^{3+}}$ values of 0.19–0.24, and some have rare earth element (REE)-richer cores (up to 5 wt %). Ilmenite occurs both as inclusions in garnet and as discrete grains in the matrix, and both cases display elevated MnO contents (2 and 3 wt %).

The metasandstone comprises muscovite-phengite (Table 3), quartz, albite (An_{0-2}), calcite, K-feldspar (X_{Or} ~ 0.95–0.96), biotite (X_{Mg} ~ 0.72–0.74; Ti

https://doi.org/10.1017/S0016756810001020 Published online by Cambridge University Press

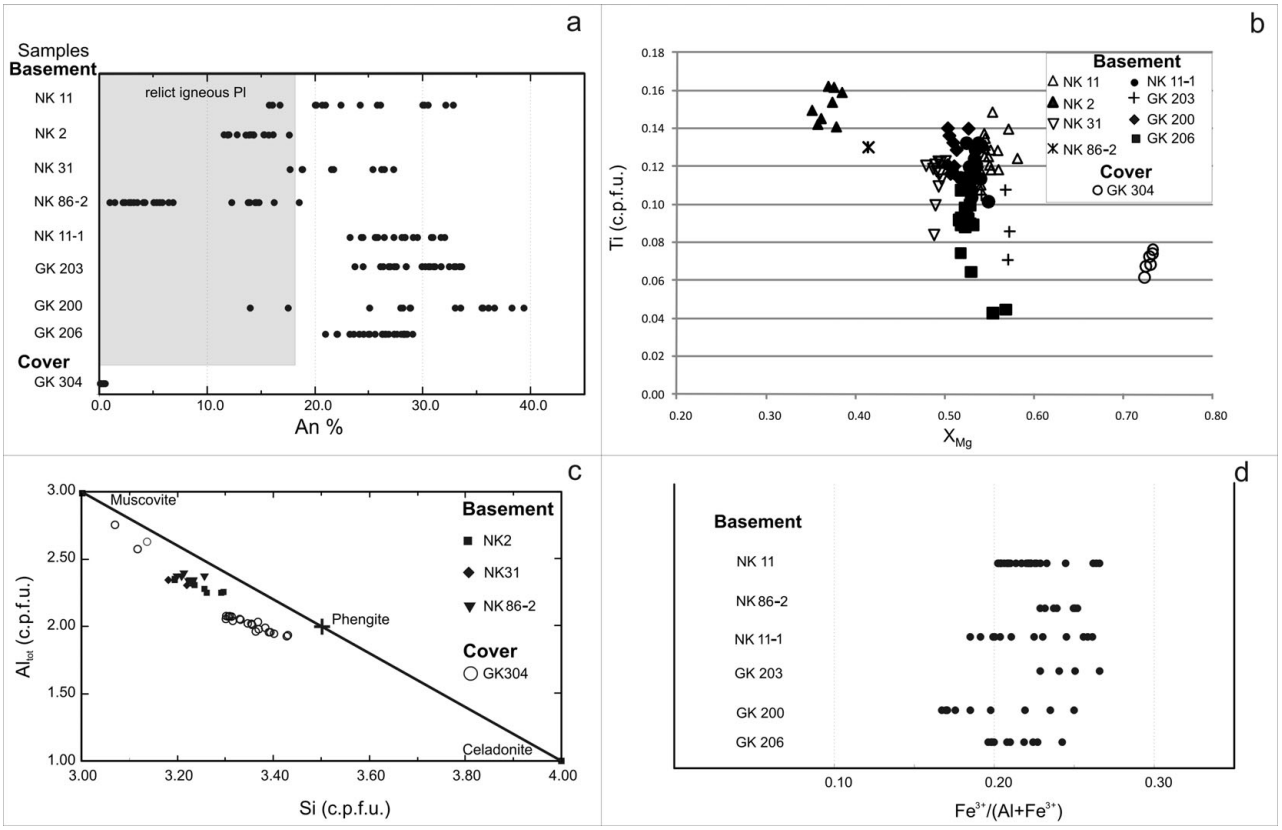

Figure 3. (a) Compositional variation of plagioclases from the basement orthogneisses and schists (epidote–amphibolites), and the cover schists (greenschists). (b) Chemical variation of biotites from the basement orthogneisses and schists (epidote–amphibolites), and the cover schists (greenschists). (c) Variation of (Al_{tot}) v. Si in K-white micas from the basement orthogneisses and schists (epidote–amphibolites), and the cover schists (greenschists). (d) Epidote compositions ($X_{Fe^{3+}}$) from the basement orthogneisses and schists (epidote–amphibolites).

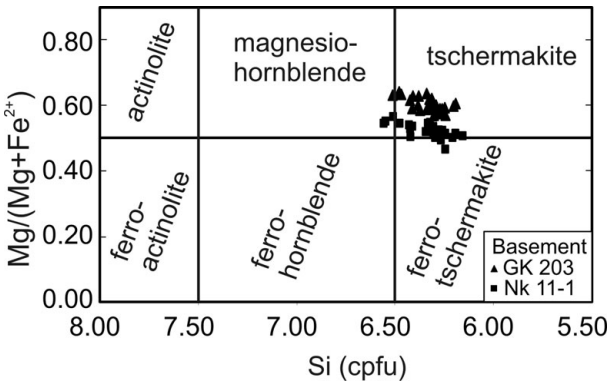

Figure 4. Amphibole compositions of the basement amphibolites (samples NK11–1 and GK203).

~0.06–0.08 cations per formula unit (cpfu; Table 3) and accessory apatite, zircon and titanite. Albite displays multiple twinning and locally forms large grains. Large grains of muscovite form bent and kinked crystals, and are relict detrital grains (Fig. 5e) displaying Si contents of 3.0–3.15 cations per 11 oxygens (Fig. 3c). However, finer-grained muscovites are represented by phengites (Si = 3.25–3.45 cations per 11 oxygens), defining the foliation, and locally have relict muscovite cores (Fig. 5e, f).

Mylonites within the Kırklareli metagranite (Fig. 2) differ from the host rocks by their well-foliated nature and fine grain sizes (~200 μm). Mineral constituents are quartz, plagioclase, K-feldspar, biotite, muscovite and minor epidote and titanite. The mylonites in the northern part are devoid of biotite (Fig. 2). Porphyroblasts are rare, and quartz and feldspar have nearly the same grain sizes. Muscovites locally form fish. Grain boundaries are lobate to cuspate. These textural features suggest that the mylonitization occurred under relatively high temperature conditions (≥400 °C) (Passchier & Trouw, 1996, p. 52).

Overall, plagioclases, muscovites, epidotes and garnets display wide intra-sample compositional variations owing to the presence of relics from the former igneous and/or metamorphic stage (Figs 3, 6).

4. Metamorphic conditions

On the basis of the arguments outlined above, it was suggested that portions of the basement sequence were subjected to a pre-Triassic metamorphism during the Early Permian (Okay *et al*. 2001; Natal'in *et al*. 2005). Here we try to constrain the *P–T* conditions of the latest metamorphism, rather than the pre-Triassic one, even though the samples also contain relict minerals from former igneous and metamorphic stages

https://doi.org/10.1017/S0016756810001020 Published online by Cambridge University Press

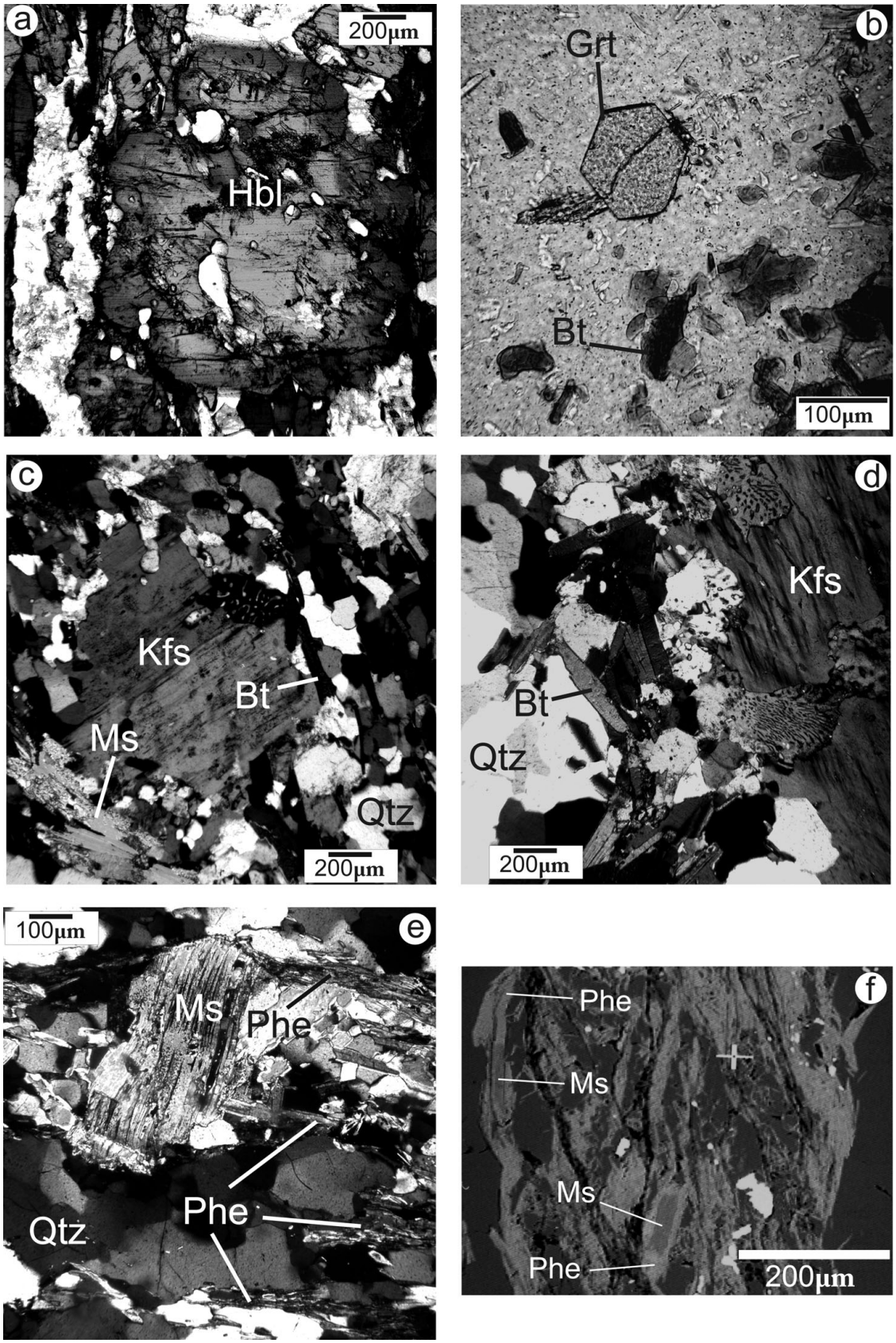

Figure 5. Photomicrographs illustrating microtextural features of micaschists, orthogneisses, amphibolites and metasandstones. (a) A large hornblende grain with inclusions of plagioclase, quartz and epidote in amphibolite (sample GK203, crossed polarized). (b) An idioblastic garnet grain in a matrix consisting of plagioclase, biotite, quartz and epidote (sample GK206, plane polarized). (c), (d) Relict feldspar grains with myrmekites in biotite–muscovite orthogneiss (Kırklareli metagranite, sample NK86–2, crossed polarized). (e) Relict large muscovite grain is bent and finer-grained phengites overgrow the muscovite grain. Note that the finer-grained phengites define the foliation (sample GK304, crossed polarized). (f) Some fine-grained phengite-rich white micas have relict cores of muscovite (sample GK304, back-scattered electron image). Bt – biotite; Grt – garnet; Hbl – hornblende; Kfs – k-feldspar; Ms – muscovite; Phe – phengite; Qtz – quartz.

https://doi.org/10.1017/S0016756810001020 Published online by Cambridge University Press

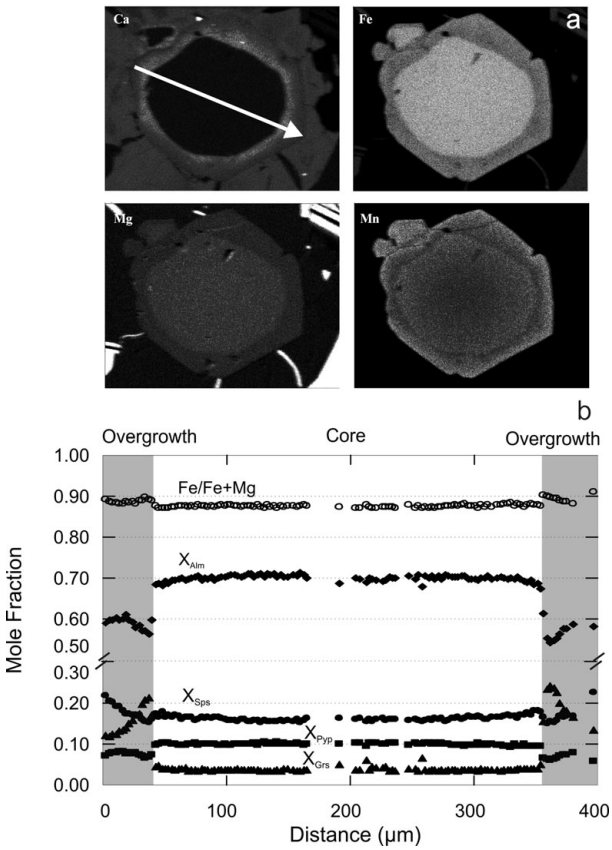

Figure 6. (a) Ca, Fe, Mg and Mn chemical imaging of a garnet from the basement schists (sample GK206). Note that line with arrow indicates chemical profile. (b) Compositional profile across garnet grain from the basement schists shown in (a) (representative analyses are given in Table 2). For a colour version of this figure see online Appendix at http://journals.cambridge.org/geo.

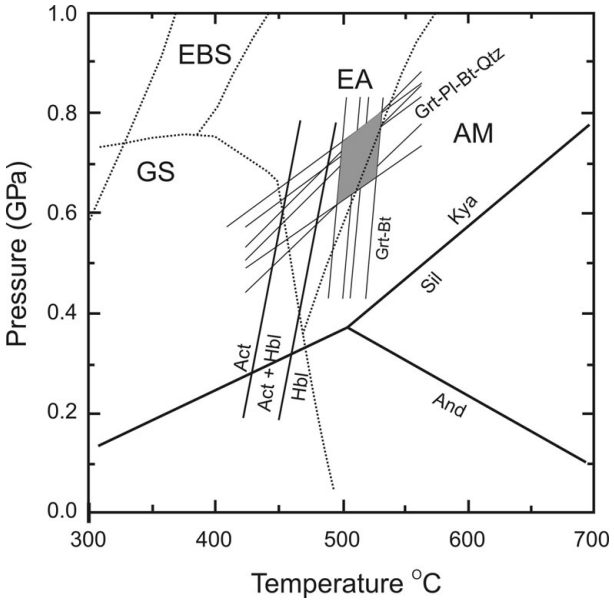

Figure 7. Combination of individual *P–T* estimates deduced for the basement unit from sample GK206. Actinolite–hornblende transition according to Baker (1990). Approximate boundaries between metamorphic facies are shown as dotted lines: GS – greenschist facies; EBS – epidote–blueschist facies; EA – epidote–amphibolite facies; AM – amphibolite facies (Krogh, Oh & Liou, 1994 and references therein).

(e.g. Alm–Sps-rich garnet cores, Ab-rich plagioclase cores and muscovite-rich cores in the white micas).

The metamorphic mineral assemblages in the amphibolites and orthogneisses (pre-Triassic basement) are characterized by the stable coexistence of plagioclase ($An_{17–35}$) + epidote ± hornblende ± quartz, suggestive of epidote–amphibolite-facies conditions (e.g. Miyashiro, 1993, pp. 280–7). In these rock types, the metamorphic plagioclases are represented by $An_{17–35}$, suggesting that the metamorphic conditions exceeded the peristerite gap (Laird, 1982; Maruyama, Liou & Suzuki, 1982). However, the metasandstone sample GK304 (Triassic cover) comprises the mineral assemblage biotite + muscovite + K-feldspar + albite + quartz + calcite, which can occur in the greenschist or albite–epidote–amphibolite facies, a transitional facies between greenschist- and epidote–amphibolite-facies (e.g. Maruyama, Suzuki & Liou, 1983; Topuz *et al.* 2004).

In general, the mineral assemblages documented are not very suitable for placing 'tight' constraints on the *P–T* conditions. However, some constraints on the *P–T* conditions could be placed from the mineral assemblages in the garnet–biotite schist (sample GK206) and amphibolite (samples NK11-1 & GK203).

Metamorphic temperatures are estimated by garnet–biotite and hornblende–plagioclase thermometry, and metamorphic pressures by garnet–biotite–plagioclase–quartz barometry. Compositions of the matrix biotites and intermediate zones of the garnet overgrowths are used, because the garnet core domains are not in equilibrium with the matrix biotite, and we do not have any constraint on the mineral assemblage present during the growth of the garnet cores. The computer program GTB provided by Spear & Kohn (1999) was used for *P–T* estimation calculations. Garnet–biotite thermometry according to the formulation of Ferry & Spear (1978) together with the garnet solution model after Berman (1990) yields a temperature of 510 ± 20 °C (2σ), and the garnet–biotite–plagioclase–quartz barometry after Hoisch (1991, 1992) gives a pressure of 0.70 ± 0.10 GPa (2σ; Fig. 7).

Hornblende–plagioclase thermometry after Spear (1980, 1981) for the adjacent hornblende–plagioclase compositions consistently yields temperatures of 485–540 °C, which are in agreement with the garnet–biotite temperatures (Fig. 8).

The *P–T* conditions for the northernmost domain are poorly defined. The metasandstones (e.g. sample GK304) contain a high-variance mineral assemblage biotite + muscovite + K-feldspar + albite + quartz + calcite. Presence of primary calcite in the assemblage suggests that the bulk composition of the protolith was not Ca-free, and accordingly the peristerite gap was not crossed. The uncrossed nature of peristerite gap and presence of biotite might indicate lower metamorphic conditions.

https://doi.org/10.1017/S0016756810001020 Published online by Cambridge University Press

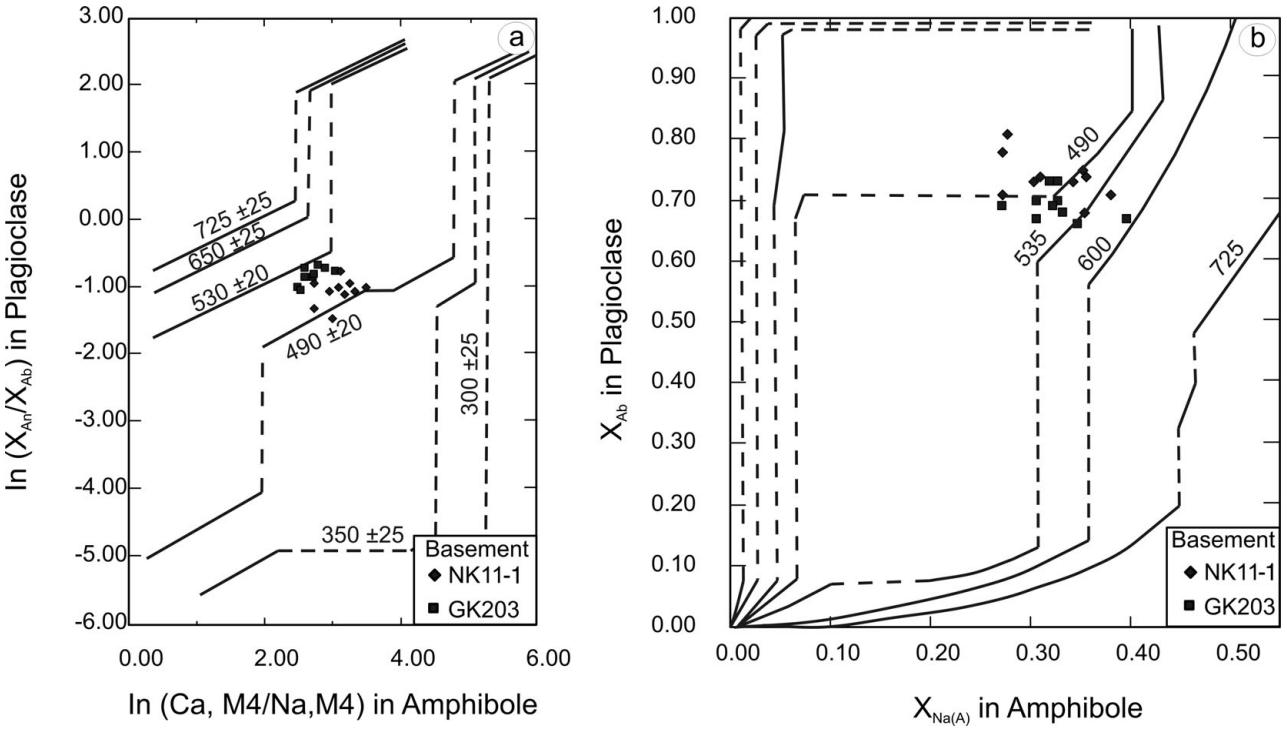

Figure 8. Temperature estimates of the basement amphibolites (Spear, 1980, 1981).

5. Geochronology

To constrain the time of medium-grade metamorphism and cooling history of the region, Rb–Sr biotite and muscovite whole-rock dating was performed on 21 samples distributed over the whole area (Fig. 2). During the sample selection, the criteria such as (i) uniform distribution of the samples throughout the study area, (ii) freshness of the dated samples, and (iii) modal contents of the samples (biotite and/or muscovite) were taken into account.

Mineral separation (biotite, muscovite) was carried out using conventional techniques including crushing, sieving, a magnetic separator and heavy liquids. The dated fractions were between 125 and 180 μm in every dated sample. Rb–Sr isotopic analyses were performed with a FINNIGAN MAT-262 multicollector mass spectrometer in Tübingen. Rb and Sr contents of whole rocks were determined by X-ray fluorescence, using lithium borate fusion discs with an accuracy better than 2 %. Rb and Sr concentrations of mineral separates were determined by isotopic dilution. Sr and light rare earth elements (LREE) were isolated on quartz columns by conventional ion exchange chromatography with a 5 ml resin bed of Bio Rad AG 50W-X12, 200–400 mesh. Sr was loaded with a Ta–HF activator on preconditioned W filaments and was measured in single-filament mode. Analyses of 28 separate loads of the NBS987 Sr standard yielded a $^{87}Sr/^{86}Sr$ ratio of 0.710259 ± 0.000012. Total procedural blanks were < 200 pg for Sr that were loaded with a Si-gel onto a preconditioned Re filament and measured at ~ 1300 °C in single-filament mode. Age determinations are based on a ^{87}Rb decay constant of 1.42×10^{-11}/yr (Steiger & Jäger, 1977). Fractionation was corrected by normalizing the $^{86}Sr/^{88}Sr$ ratios to 0.1194. The input errors for age computations are 1 % (2σ) for $^{87}Rb/^{86}Sr$ ratios and 0.003 % (2σ) for $^{87}Sr/^{86}Sr$ ratios (see Siebel *et al*. 2005 for a detailed discussion). The Rb–Sr mineral whole-rock isochron age calculations were performed using the Isoplot 3.0 program produced by Ludwig (2003). For the interpretation of the ages provided in this study, it should be kept in mind that they contain only mineral and whole-rock data, in other words ages calculated using the two-point isochron method, which represent apparent ages. Two-point isochron calculations always reveal low error values that are mainly based on an assigned a priori Rb/Sr error of 1 %. The two-point isochron approach inherently assumes initial isotopic equilibrium among all phases of a rock, which may or may not be correct for a given rock. If isotopic equilibrium has not been achieved during a geological process, such a two-point isochron age is at risk of deviating from the true age of the process, and the true uncertainty on the age may be underestimated by the formal calculation of age errors from the two data points.

The Rb–Sr biotite ages range from 153.9 ± 1.5 Ma (2σ) in the south to 134.4 ± 1.3 Ma (2σ) in the north (Fig. 9; Table 5). The Rb–Sr muscovite ages cluster mostly between 157.7 ± 1.5 and 162.3 ± 1.6 Ma. However, two samples (MS1 and GK134) yielded outlier age values of 149.6 ± 1.5 Ma and 149.1 ± 2.1 Ma. However, the muscovites from the northernmost portion yielded considerably older age values between 279.2 ± 3.0 and 295.6 ± 2.8 Ma (Fig. 9). The Rb–Sr biotite ages are similar to the

https://doi.org/10.1017/S0016756810001020 Published online by Cambridge University Press

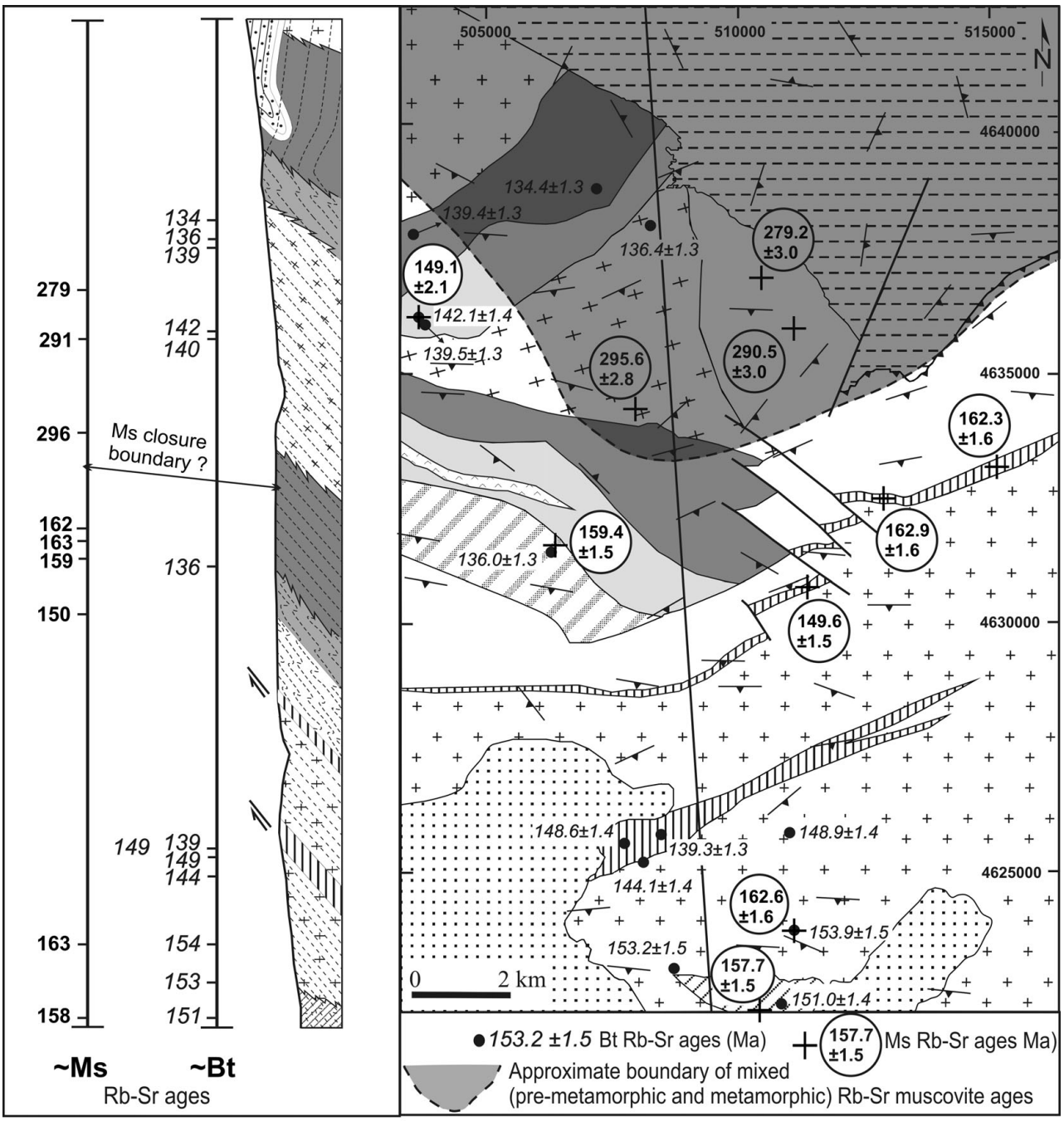

Figure 9. Distribution of Rb–Sr biotite (Bt) and muscovite (Ms) ages in the study area and alignment of them on a roughly S–N directed cross-section. Coordinates are UTM, European (ED50) and Zone 35.

previously published scarce K–Ar biotite and Rb–Sr biotite ages (Okay *et al*. 2001; Lilov & Maliakov, 2001; Lilov, Maliakov & Balogh, 2004).

Pb–Pb zircon evaporation data on the orthogneisses on the same rock types revealed that their igneous protoliths were formed between 315 and 256 Ma (Okay *et al*. 2001; Natal'in *et al*. 2005; Sunal *et al*. 2006) and the micaschists contain detrital zircons with age intervals of 430–2700 Ma (garnet–biotite schist) and 300–350 Ma (biotite schist). Cathodoluminescence (CL) images revealed the presence of small metamorphic overgrowths on the zircons, which, however, could not be dated by the Pb–Pb evaporation method (Sunal *et al*. 2008). On the other hand, the Rb–Sr systematics on biotite and muscovite apart from the 'older' ages (279–295 Ma) should refer to the latest metamorphic event in the Strandja Massif.

6. Discussion

6.a. Meaning of mineral isochron ages

The closure temperature is a complex function of several factors such as solid-state diffusion parameters, effective grain size, temperature, cooling rate, fluid activity, deformation and surrounding exchange medium

https://doi.org/10.1017/S0016756810001020 Published online by Cambridge University Press

Table 5. Results of Rb–Sr dating on muscovite and biotite separates

Sample	Rb (μg/g)	Sr (μg/g)	$^{87}Rb/^{86}Sr$	$^{87}Sr/^{86}Sr \pm 2\sigma$	Age (Ma) ± Error (Ma)	Sample description	Coordinates Latitude	Coordinates Longitude
Kırklareli metagranite								
K1(WR)	233	77	8.710	0.738796 ± 10		wkf, Q+Kfs+Pl+Bt+Ms+Ep+Zrn	508990	4623153
K1(Bt)	1215	3	1084.204	3.080426 ± 9	153.2 ± 1.5*	+Ap		
K2(WR)	161	101	4.592	0.724478 ± 12		f, Q+Kfs+Pl+Bt+Ms+Ep+Chl	511372	4623913
K2(Bt)	1050	2	1339.926	3.646080 ± 12	153.9 ± 1.5*	+Zrn+Ap		
K2(Ms)	599	7	247.313	1.285593 ± 11	162.6 ± 1.6*			
K3(WR)	189	83	6.586	0.731029 ± 8		wlf, Q+Kfs+Pl+Bt+Ms+Ep+Zrn	511279	4625855
K3(Bt)	1077	2	1917.151	4.773714 ± 10	148.9 ± 1.4*	+Ap+Ttn		
Hbl–Bt granite gneiss								
HBG1(WR)	37	218	0.50	0.710005 ± 10		f, Hbl+Pl+Bt+Q+Ep+Cal+Chl	503593	4636142
HBG1(Bt)	312	3	258.780	1.221822 ± 9	139.4 ± 1.3*	+Zrn+Ap+Ttn+Ilm		
HBG2(WR)	66	337	0.568	0.710675 ± 8		f, Hbl+Pl+Bt+Q+Ep+Cal+Chl	507050	4638428
HBG2(Bt)	359	1	597.119	1.850316 ± 10	134.4 ± 1.3*	+Zrn+Ap+Ttn+Ilm+Grt		
White mylonitic gneiss								
WMG1(WR)	274	64	12.432	0.763225 ± 10		wlf, Q+Pl+Ms+Kfs+Ep+Zrn	511130	4635883
WMG1(Ms)	728	15	146.230	1.316260 ± 9	290.5 ± 3.0*	+Ap+Ttn		
WMG2(WR)	223	49	13.113	0.763604 ± 9		wlf, Q+Pl+Ms+Kfs +Ep+Zrn	510484	4636919
WMG2(Ms)	719	19	114.102	1.164795 ± 10	279.2 ± 3.0*	+Ap+Ttn		
Biotite schist (north)								
MS1(WR)	62	286	0.633	0.715350 ± 10		wlf, Q+Pl+Bt+Kfs+Ep+Ms+Chl	503930	4636108
MS1(Bt)	473	4	328.836	1.378453 ± 12	142.1 ± 1.4*	+Zrn+Ap+Ttn		
MS1 (Ms)	208	57	10.531	0.736328 ± 10	149.1 ± 2.1*			
MS2(WR)	188	307	1.772	0.714919 ± 9		wlf, Q+Pl+Bt+Kfs+Ep+Ms+Chl	504059	4635956
MS2(Bt)	389	8	142.262	0.993520 ± 9	139.5 ± 1.3*	+Zrn+Ap+Ttn+Grt		
Biotite schist (south)								
MS3(WR)	116	213	1.577	0.714517 ± 8		wlf, Q+Pl+Bt+Kfs+ Ep+Ms+Chl	510723	4622332
MS3(Ms)	364	17	61.191	0.848146 ± 10	157.7 ± 1.5*	+Hbl+Zrn+Ap		
MS4(WR)	39	510	0.226	0.707188 ± 12		wlf, Q+Pl+Bt+Kfs+ Ep+Ms+Chl	511117	4622449
MS4(Bt)	373	6	165.143	1.061114 ± 9	151.0 ± 1.4*	+Zrn+Ap		
Bt–Ms granite gneiss								
BMG1(WR)	128	176	2.105	0.721414 ± 10		wkf, Q+Kfs+Pl+Bt+Ms+Ep+Zrn	507927	4634085
BMG1(Ms)	602	13	135.508	1.282625 ± 11	295.6 ± 2.8*	+Ap+Ttn		
BMG2(WR)	92	245	1.087	0.714743 ± 11		wkf, Q+Kfs+Pl+Bt+Ms+Ep+Zrn	508521	4637933
BMG2(Bt)	412	20	57.910	0.824941 ± 7	136.4 ± 1.3*	Ap+Ttn		
Bt mylonite								
GK127(WR)	101	135	2.179	0.714944 ± 10		vwlf, Q+Pl+Kfs+Bt+Ep+Ms+Zrn	508383	4625267
GK127(Bt)	680	5	424.244	1.579272 ± 9	144.1 ± 1.4	+Ap+Ttn		
GK128(WR)	84	430	0.571	0.709319 ± 10		vwlf, Q+Pl+Kfs+Bt+Ep+Ms+Zrn	508733	4625818
GK128(Bt)	502	15	97.586	0.901420 ± 10	139.3 ± 1.3	+Chl+Ttn		
GK129(WR)	92	448	0.594	0.709374 ± 10		vwlf, Q+Pl+Kfs+Bt+Ep+Zrn	508006	4625643
GK129(Bt)	598	10	173.446	1.074460 ± 9	148.6 ± 1.4	+Chl+Ap		
GK131(WR)	81	455	0.521	0.710099 ± 8		vwlf, Q+Pl+Kfs+Bt+Ep+Ms+Zrn	506555	4631432
GK131(Bt)	547	8	194.998	1.085982 ± 12	136.0 ± 1.3	+Ap		
Ms mylonite								
GK130(WR)	166	89	5.397	0.730247 ± 10		vwlf, Q+Pl+Kfs+Ms+Ep+Bt+Chl	506641	4631578
GK130(Ms)	540	10	159.948	1.080387 ± 12	159.4 ± 1.5	+Zrn+Ttn		
GK134(WR)	199	93	6.203	0.733686 ± 12		vwlf, Q+Pl+Kfs+Ms+Ep+Chl	511399	4630377
GK134(Ms)	562	19	84.150	0.899454 ± 8	149.6 ± 1.5	+Grt+Zrn+Ttn		
GK135(WR)	111	93	3.477	0.727350 ± 9		vwlf, Q+Pl+Kfs+Ms+Ep+Zrn+Ap	512816	4631942
GK135(Ms)	546	35	45.482	0.824641 ± 9	162.9 ± 1.6			
GK136(WR)	104	284	1.067	0.711537 ± 10		vwlf, Q+Pl+Kfs+Ms+Ep+Bt+Zrn	515264	4633043
GK136(Ms)	542	74	21.224	0.758051 ± 11	162.3 ± 1.6	+Ap		

WR – whole-rock, Bt – biotite, Ms – muscovite, Hbl – hornblende, vwlf – very well foliated, wlf – well foliated, wkf – weakly foliated, f – foliated, Q – quartz, Pl – plagioclase, Kfs – potassium feldspar, Ep – epidote, Chl – chlorite, Cal – calcite, Grt – garnet, Zrn – zircon, Ap – apatite, Ttn – titanite, Ilm – ilmenite. Coordinates are UTM (ED50), Zone 35.
*Ages recalculated after O. Vonderschmidt (unpub. M.Sc. thesis, Univ. Tübingen, 2004) according to the following errors; 2σ error on $^{87}Rb/^{86}Sr$ is 1 %; 2σ error on $^{87}Sr/^{86}Sr$ is 0.003 %. Errors are given as 95 % confidence limit.

(Dodson, 1973; Villa, 1998; Montel, Kornprobst & Vielzeuf, 2000; Müller, Aerden & Halliday, 2000; Kühn *et al*. 2000; Glodny *et al*. 2003, 2005; Reddy *et al*. 2003; Glodny, Kühn & Austrheim, 2008). Absence of a free fluid phase and of suitable minerals with which the micas can exchange Sr may strongly increase closure temperature (Kühn *et al*. 2000; Glodny, Kühn & Austrheim, 2008). However, in our sample set, the presence of synkinematic quartz veins indicates fluid activity during deformation. Besides, the dated samples are well-foliated and contain epidote and apatite. The epidote and apatite in free fluid-bearing environments can act as a large Sr reservoir with which the micas can exchange Sr (Zeck & Hansen, 1988; Glodny, Kühn & Austrheim, 2008). The Rb–Sr age difference between the biotite ages in the south and those in the north is ∼ 15 Ma, which cannot be accounted for by the analytical uncertainty, usually in the order of 1 to 3 Ma (95 % confidence level (2σ)). The biotite ages are thus best explained as dating

https://doi.org/10.1017/S0016756810001020 Published online by Cambridge University Press

their Sr-isotopic closure at fluid-present conditions, at temperatures in the range of ~300 to 400 °C (Purdy & Jäger, 1976; Giletti, 1991; Del Moro *et al*. 1982). The biotite ages date a stage of greenschist-facies conditions during post-metamorphic exhumation of the Strandja Massif.

Given that estimated metamorphic peak temperatures were near the commonly assumed isotopic closure temperature of muscovite for Sr diffusion (~500 °C), we interpret the muscovite ages from the southern and central parts of the study area as dating either synmetamorphic deformation (e.g. Freeman *et al*. 1997) or a very early stage of postkinematic cooling (between 157.7 ± 1.5 and 162.3 ± 1.6 Ma). A clear distinction between these two options is impossible. In any case, these muscovite ages date a near-peak stage of Middle to Late Jurassic metamorphism. The pre-Jurassic ages from the northern part of the study area (apparent ages between 279 ± 3.0 and 295 ± 2.8 Ma) are interpreted as mixed ages, because the dated samples contain both relict igneous and metamorphic muscovite (Figs 5e, f). The apparent ages give a minimum age for igneous muscovite crystallization and a maximum age for the muscovite-forming metamorphism.

6.b. Geodynamic significance

The section of the Strandja Massif in the study area has Palaeozoic basement rocks with Triassic cover units. The cover consists of a transgressive sequence that starts with metaconglomerates at the base and reaches marbles (not observed in the studied part) at the top of the section. This sequence was interpreted as epi-continental by Okay *et al*. (2001). However, Chatalov (1991) reported an allochthonous Triassic sequence in the Bulgarian section of the massif that comprises greenschist-facies phyllites and metabasites. This unit was formerly interpreted as an accretionary complex (e.g. Şengör, Yılmaz & Sungurlu, 1984). Okay *et al*. (2001) interpreted this allochthonous Triassic sequence as the main reason for regional metamorphism occurring in the Strandja Massif.

As revealed by the study presented here, the Middle Mesozoic cooling in the Strandja Massif displays a significant diachronism. The tectonic event controlling the metamorphism and subsequent cooling/exhumation propagated northward between Late Jurassic and Early Cretaceous time. Diachronous cooling was described from different tectonic settings such as compressional (e.g. Boyle, Burton & Westhead, 1994; Dallmeyer *et al*. 1997; Crowley & Parrish, 1999; Gray *et al*. 2006; Tricart *et al*. 2007; Jeřábek *et al*. 2008), extensional (e.g. Holm & Dokka, 1993; Bertrand *et al*. 2001) and transpressional segments of strike-slip systems (Morillon *et al*. 2000; Koons *et al*. 2003). In the case of the Strandja Massif, compression led to overturned folding and thrusting, deduced from (i) the occurrence of the cover sequence beneath the basement (Fig. 9), (ii) an inverse metamorphic gradient, and (iii) top-to-the-N ductile shear zones (Natal'in *et al*. 2005; Natal'in, Sunal & Toraman, 2005).

Pressure estimates obtained in this study indicate that during the deformation, the Strandja Massif was buried to depths of 22–29 km. The oldest non-metamorphic rocks unconformably resting on the Strandja Massif are represented by earliest Late Cretaceous sandstones (Cenomanian, ~ 95 Ma, Okay *et al*. 2001; Türkecan & Yurtsever, 2002) on the northern flank and an Eocene–Oligocene sequence of limestone, sandstone and shale on the southern flank (Çağlayan, Şengün & Yurtsever, 1988). This suggests that at least parts of the Strandja Massif were at the Earth's surface before 95 Ma. It should be noted that erosion was also a contributing mechanism for exhumation in the Strandja Massif. During Early Cretaceous time, a nearly E–W-trending depositional basin was present on the Moesian, parts of the Sredna Gora zone and the Strandja Massif (Minkovska, Peybernès & Nikolov, 2002; Fig. 1). The southern margin of this basin is represented mainly by up to 4000 m thick flysch-type coarse siliciclastics, while the northern margin is made up of a considerably wider shallow water carbonate platform. This suggests significant clastic input from the south, namely from the Strandja and probably parts of the Rhodopes.

There are several tectonic zones and massifs surrounding the Strandja Massif, but their palaeotectonic position and geological relationships with the Strandja Massif are not clear because of the subsequent geological deformation phases that destroyed most of the older structures. Two different zones have been identified to the N and NW of the Strandja Massif: the Sredna Gora and the Balkan zones (Chatalov, 1988; Yanev, 2000). The Sredna Gora zone mainly consists of Upper Cretaceous unmetamorphosed volcanics. The Balkan zone has the same Late Palaeozoic basement as the Strandja Massif but it is not metamorphosed either (Carrigan *et al*. 2005; Sunal *et al*. 2006). The Rhodopes, the Circum-Rhodope Belt and small metamorphic domains in southern Thrace and Biga Peninsula are located to the S and SW of the Strandja Massif (Fig. 1). In contrast to the Strandja Massif, these metamorphic domains locally contain rock assemblages that suggest involvement in accretion and subduction events (e.g. Okay & Satır, 2000; Mposkos & Krohe, 2006; Bonev, Marchev & Singer, 2006; Bauer *et al*. 2007; Topuz *et al*. 2008). The timing of the high *P–T* metamorphism in southern Thrace and the Biga Peninsula is estimated to be Late Cretaceous (Okay & Satır, 2000; Topuz *et al*. 2008). The relationship between the Strandja and the Rhodope massifs during the Late Jurassic to Early Cretaceous interval is still a matter of conjecture (Fig. 1). For example, Gerdjikov & Gautier (2005) and Gerdjikov (2005) have discussed the absence of a known suture zone between these two units. Both regions have similar basement geology having Permo-Carboniferous granitoids of the Variscan event (Cherneva & Georgieva, 2005; Carrigan *et al*. 2005; Liati & Fanning, 2005; Sunal *et al*. 2006) and mid-Mesozoic

https://doi.org/10.1017/S0016756810001020 Published online by Cambridge University Press

metamorphism (Liati, 2005; Bauer *et al*. 2007; Bonev *et al*. 2009), but rock types and grades of metamorphism differ from each other. Metamorphism in the Rhodope massif reveals mainly high- to ultrahigh-pressure conditions (Mposkos & Krohe, 2006; Bauer *et al*. 2007) that form as a result of northward subduction of the Nestos Ocean (e.g. Ricou, 1994). Recent geochronological data consistently suggest that the timing of high- to ultrahigh-pressure metamorphism in the Rhodopes is at ≥160 Ma (e.g. Mposkos & Krohe, 2006; Bauer *et al*. 2007). Furthermore, the time of retrogression of high- to ultrahigh facies to amphibolite facies is given as *c*. 144 Ma (Krenn *et al*. 2007). This retrogression is linked with unroofing of the eclogites via extensional tectonics (Krenn *et al*. 2007). In the Balkan region, at least in terms of timing of the metamorphic events, the Rhodope Massif seems to be geologically related to the Strandja Massif. However, the relationship between the Strandja and the Rhodope massifs is obscured by subsequent geological events that make it difficult to reconstruct a Mesozoic tectonic framework, such as (i) Tertiary metamorphic overprint in the Rhodopes, (ii) later strike-slip faults that formed between these metamorphic massifs, and (iii) the Tertiary basin that developed on both the Strandja and the Rhodope massifs. In Bulgaria, a pronounced right-lateral strike-slip fault, i.e. the Maritsa fault zone (MFZ in Fig. 1), with an offset of over 100 km, is located between the Strandja and the Rhodope massifs (Burg *et al*. 1996; Ivanov, 2000). The elongation of the Maritsa fault into Turkey is concealed in the Pliocene sedimentary rocks of the Thrace basin (c.f. Perinçek, 1991; Yaltırak, 2002). The Turkish section of the fault is known as the Thrace–Eskişehir Fault Zone (TEFZ in Fig. 1) that was thought to be active between the Early Miocene and Pliocene (Yaltırak, 2002). Despite these difficulties, the compressional deformation in the Strandja Massif seems very likely related to the northward subduction and accretion events in the Rhodopes that occurred during Late Jurassic to Early Cretaceous time.

7. Conclusions

The southern part of the Strandja Massif, NW Turkey, comprises a basement of various orthogneisses, micaschists and amphibolites, and an epiclastic cover of metaconglomerate and metasandstone. Both sequences underwent a transitional greenschist- to epidote–amphibolite-facies metamorphism in a compressional regime during Late Jurassic to Early Cretaceous time. The ages of peak or near-peak metamorphism are clustered between 157.7 ± 1.5 and 162.3 ± 1.6 Ma and subsequent cooling occurred diachronously between 153.9 ± 1.5 Ma and 134.4 ± 1.3 Ma, starting in the south and progressing to the north. The compressional regime probably resulted from thrusting and overturned folding, and was ultimately related to the coeval subduction and collision events in the southerly Rhodope Massif.

Acknowledgements. This paper forms a part of the Ph.D. thesis of G. Sunal at the University of Tübingen. Field work and travel expenses were funded by ITU Research fund (#11-07-128) and TÜBITAK (The Scientific and Technical Research Council of Turkey, Project no: YDABCAG 101Y010). The help of G. Bartholomä during mineral separation, and W. Siebel and E. Reitter during isotopic measurements is gratefully appreciated. Early drafts of the manuscript were reviewed by A. I. Okay, P. Bons and W. Siebel, which led to considerable improvement of the ideas. We thank R. Altherr for friendly access to the electron microprobe facility in Heidelberg. Insightful and constructive reviews were provided by U. Ring and two anonymous referees.

References

BAKER, A. J. 1990. *Introduction to Metamorphic Textures and Microstructures*. New York: Blackie, 162 pp.

BAUER, C., RUBATTO, D., KRENN, K., PROYER, A. & HOINKES, G. 2007. A zircon study from the Rhodope Metamorphic Complex, N-Greece: time record of a multistage evolution. *Lithos* **99**, 207–28.

BERMAN, R. G. 1990. Mixing properties of Ca-Mg-Fe-Mn garnets. *American Mineralogist* **75**, 328–44.

BERTRAND, G., RANGIN, C., MALUSKI, H. & BELLON, H. 2001. Diachronous cooling along the Mogok Metamorphic Belt (Shan Scarp, Myanmar): the trace of the northward migration of the Indian syntaxis. *Journal of Southeast Asian Earth Sciences* **1**, 649–59.

BONEV, N., MARCHEV, P. & SINGER, B. 2006. $^{40}Ar/^{39}Ar$ geochronology constraints on the Middle Tertiary basement extensional exhumation, and its relation to ore-forming and magmatic processes in the eastern Rhodope (Bulgaria). *Geodinamica Acta* **19**, 267–82.

BONEV, N., MORITZ, R., MÁRTON, I., CHIARADIA, M. & MARCHEV, P. 2010. Geochemistry, tectonics, and crustal evolution of basement rocks in the Eastern Rhodope Massif, Bulgaria. *International Geology Review* **52** (2–3), 269–97.

BOYLE, A. P., BURTON, K. W. & WESTHEAD, R. K. 1994. Diachronous burial and exhumation of a single tectonic unit during collision orogenesis (Sulitjelma, central Scandinavian Caledonides). *Geology* **22**, 1043–6.

BURG, J. P., RICOU, L. E., IVANOV, Z., GODFRIAUX, I., DIMOV, D. & KLAIN, L. 1996. Syn-metamorphic nappe complex in the Rhodope Massif: structure and kinematics. *Terra Nova* **8**, 6–15.

ÇAĞLAYAN, A. M., ŞENGÜN, M. & YURTSEVER, A. 1988. Main fault systems shaping the Istranca Massif, Turkey. *Journal of Pure and Applied Science, Series A, Geosciences*. **21**, 145–54.

CARRIGAN, C. W., MUKASA, S. B., HAYDOUTOV, I. & KOLCHEVA, K. 2005. Age of Variscan magmatism from the Bulgarian sector of the orogen. *Lithos* **82**, 125–47.

CHATALOV, G. 1988. Recent developments in the geology of the Strandja Zone in Bulgaria. *Bulletin of the Technical University of Istanbul* **41**, 433–66.

CHATALOV, A. G. 1991. Triassic in Bulgaria – a review. Special issue on tectonics (ed. J. F. Dewey). *Bulletin of the Technical University of Istanbul* **44** (1–2), 103–35.

CHERNEVA, Z. & GEORGIEVA, M. 2005. Metamorphozed Hercynian granitoids in the Alpine structures of the Central Rhodope, Bulgaria: geotectonic position and geochemistry. *Lithos* **82**, 149–68.

CROWLEY, J. L. & PARRISH, R. R. 1999. U-Pb isotopic constraints on diachronous metamorphism in the

northern Monashee complex, southern Canadian Cordillera. *Journal of Metamorphic Geology* **17**, 483–502.

DALLMEYER, R. D., MARTÍNEZ CATALÁN, J. R., ARENAS, R., GIL IBARGUCHI, J. I., GUTIÉRREZ ALONSO, G., FARIAS, P., BASTIDA, F. & ALLER, J. 1997. Diachronous Variscan tectonothermal activity in the NW Iberian Massif: evidence from $^{40}Ar/^{39}Ar$ dating of regional fabrics. *Tectonophysics* **277**, 307–37.

DEL MORO, A., PUXEDDU, M., RADICATI DI BROZOLO, F. & VILLA, I. M. 1982. Rb–Sr and K–Ar ages on minerals at temperatures of 300°–400 °C from deep wells in the Larderello geothermal field (Italy). *Contributions to Mineralogy and Petrology* **81**, 340–9.

DODSON, M. H. 1973. Closure temperature in cooling geochronological and petrological systems. *Contributions to Mineralogy and Petrology* **40**, 259–74.

FERRY, J. M. & SPEAR, F. S. 1978. Experimental calibration of the partitioning of Fe and Mg between biotite and garnet. *Contributions to Mineralogy and Petrology* **66**, 113–17.

FREEMAN, S. R., INGER, S., BUTLER, R. W. H. & CLIFF, R. A. 1997. Dating deformation using Rb-Sr in white micas: greenschist facies deformation ages for the Entrelor Shear Zone, Italian Alps. *Tectonics* **16**, 57–76.

GERDJIKOV, I. 2005. Alpine metamorphism and granitoid magmatism in the Strandja zone: new data from the Sakar unit, SE Bulgaria. *Turkish Journal of Earth Sciences* **14**, 167–83.

GERDJIKOV, I. & GAUTIER, P. 2005. Early alpine orogeny as recorded in metamorphic complexes of Southern Bulgaria. EGU05-A-11126. *Geophysical Research Abstracts* **7**, 11126.

GILETTI, B. J. 1991. Rb and Sr diffusion in alkali feldspars, with implications for cooling histories of rocks. *Geochimica et Cosmochimica Acta* **55**, 1331–43.

GLODNY, J., AUSTRHEIM, H., MOLINA, J. F., RUSIN, A. & SEWARD, D. 2003. Rb/Sr record of fluid–rock interaction in eclogites: the Marun-Keu complex, Polar Urals, Russia. *Geochimica et Cosmochimica Acta* **67**, 4353–71.

GLODNY, J., KÜHN,, A. & AUSTRHEIM, H. 2008. Diffusion versus recrystallization processes in Rb–Sr geochronology: isotopic relics in eclogite facies rocks, Western Gneiss Region, Norway. *Geochimica et Cosmochimica Acta* **72**, 506–25.

GLODNY, J., RING, U., KÜHN, A., GLEISSNER, P. & FRANZ, G. 2005. Crystallization and very rapid exhumation of the youngest Alpine eclogites (Tauern Window, Eastern Alps) from Rb/Sr mineral assemblage analysis. *Contributions to Mineralogy and Petrology* **149**, 699–712.

GRAY, D. R., FOSTER, D. A., GOSCOMBEC, B., PASSCHIER, C. W. & TROUWE, R. A. J. 2006. $^{40}Ar/^{39}Ar$ thermochronology of the Pan-African Damara Orogen, Namibia, with implications for tectonothermal and geodynamic evolution. *Precambrian Research* **150**, 49–72.

HAGDORN, H. & GÖNCÜOGLU, M. C. 2007. Early-Middle Triassic echinoderm remains from the Istranca Massif, Turkey. *Neus Jahrbuch für Geologie und Paläontologie Abhandlungen* **246** (2), 235−45.

HOISCH, T. D. 1991. Equilibria within the mineral assemblage quartz +muscovite + biotite + garnet + plagioclase, and implications for the mixing properties of octahedrally-coordinated cations in muscovite and biotite. *Contributions to Mineralogy and Petrology* **108**, 43–54.

HOISCH, T. D. 1992. Thermodynamic properties of muscovite and biotite: inferences from natural compositions. *Trends in Mineralogy* **1**, 107–15.

HOLM, D. K., & DOKKA, R. K. 1993. Interpretation and tectonic implications of cooling histories – an example from the Black Mountains, Death-Valley extended terrane, California. *Earth and Planetary Science Letters* **116** (1–4), 63–80.

IVANOV, Z. 2000. Tectonic position, structure and tectonic evolution of Rhodope massif. In *Guide to excursion ABCD GEODE 2000 Workshop*. Borovets, Bulgaria, pp. 1–6.

JEŘÁBEK, P., FARYAD, W. S., SCHULMANN, K., LEXA, O. & TAJČMANOVÁ, L. 2008. Alpine burial and heterogeneous exhumation of Variscan crust in the west Carpathians: insight from thermodynamic and argon diffusion modeling. *Journal of Geological Society, London* **165**, 479–98.

KONRAD-SCHMOLKE, M., O'BRIEN, P. J., DE CAPITANI, C. & CARSWELL, D. A. 2008. Garnet growth at high- and ultra-high pressure conditions and the effect of element fractionation on mineral modes and composition. *Lithos* **103**, 309–32.

KOONS, P. O., NORRIS, R. J., CRAW, D. & COOPER, A. F. 2003. Influence of exhumation on the structural evolution of transpressional plate boundaries: an example from the Southern Alps, New Zealand. *Geology* **31**, 3–6.

KRENN, K., BAUER, C., PROYER, A. & HOINKES, G. 2007. Geodynamic evolution of an UHP Suture Zone in the Greek Rhodope. *American Geophysical Union, Fall Meeting, abstract* V13A-1137.

KROGH, E. J., OH, C. W. & LIOU, J. G. 1994. Polyphase and anticlockwise P-T evolution for Franciscan eclogites and blueschists from Jenner, California, USA. *Journal of Metamorphic Geology*. **12**, 121–34.

KÜHN, A., GLODNY, J., IDEN, K. & AUSTRHEIM, H. 2000. Retention of Precambrian Rb/Sr phlogopite ages through Caledonian eclogite facies metamorphism, Bergen Arc Complex, W-Norway. *Lithos* **51**, 305–30.

LAIRD, J. 1982. Amphiboles in metamorphosed basaltic rocks. In Amphiboles (eds D. R. Veblen & P. H. Ribbe). *MSA Reviews in Mineralogy* **9B**, 113–58.

LIATI, A. 2005, Identification of repeated Alpine (ultra) high-pressure metamorphic events by U–Pb SHRIMP geochronology and REE geochemistry of zircon: the Rhodope zone of Northern Greece. *Contributions to Mineralogy and Petrology* **150**, 608–30.

LIATI, A. & FANNING, C. M. 2005. Eclogites and their country rock orthogneisses in East Rhodope representing Upper Permian gabbros and Upper Carboniferous granitoids: geochronological constraints. *Abstract Mitteilungen der Österreichischen Mineralogischen Gesellschaft* **150**, 88.

LILOV, P. & MALIAKOV, Y. 2001. Données de géochronologie isotopique sur les métadiabases du Strandja. *Comtes rendus de L'Académie bulgare des Sciences* **54**, 67–70.

LILOV, P., MALIAKOV, Y. & BALOGH, K. 2004. K-Ar dating of metamorphic rocks from Strandja massif, SE Bulgaria. *Bulgarian Academy of Sciences, Geochemistry, Mineralogy and Petrology* **41**, 107–20.

LUDWIG, K. R. 2003. *ISOPLOT 3.0. A geochronological toolkit for Microsoft Excel*. Berkeley Geochronology Center, Special Publication. No. 4.

MARUYAMA, S., LIOU, J. G. & SUZUKI, K. 1982. The peristerite gap in low-grade metamorphic rocks. *Contributions to Mineralogy and Petrology* **81**, 268–76.

MARUYAMA, S., SUZUKI, K. & LIOU, J. G. 1983. Greenschist-amphibolite transition equilibria at low pressures. *Journal of Petrology* **24**, 583–604.

MINKOVSKA, V., PEYBERNÈS, B. & NIKOLOV, T. 2002. Palaeogeography and geodynamic evolution of the Balkanides and Moesian 'microplate' (Bulgaria) during the earliest Cretaceous. *Cretaceous Research* **23**, 37–48.

MIYASHIRO, A. 1993. *Metamorphic Petrology*. London: UCL Press, 404 pp.

MONTEL, J. M., KORNPROBST, J. & VIELZEUF, D. 2000. Preservation of old U–Th–Pb ages in shielded monazite: example from Beni Bousera Hercynian kinzigites (Morocco). *Journal of Metamorphic Geology* **18**, 335–42.

MORILLON, A. C., FÉRAUD, G., SOSSON, M., RUFFET, G., CREVOLA, G. & LEROUGE, G. 2000. Diachronous cooling on both sides of a major strike slip fault in the Variscan Maures Massif (south-east France), as deduced from a detailed $^{40}Ar/^{39}Ar$ study. *Tectonophysics* **321**, 103–26.

MPOSKOS, E. & KROHE, A. 2006. Pressure–temperature–deformation paths of closely associated ultra-high-pressure (diamond-bearing) crustal and mantle rocks of the Kimi complex: implications for the tectonic history of the Rhodope Mountains, northern Greece. *Canadian Journal of Earth Sciences* **43**, 1755–76.

MÜLLER, W., AERDEN, D. & HALLIDAY, A. N. 2000. Isotopic dating of strain fringe increments: duration and rates of deformation in shear zones. *Science* **288**, 2195–98.

NATAL'IN, B. A., SATIR, M., SUNAL, G. & TORAMAN, E. 2005. Structural and metamorphic evolution of the Strandja massif. Project No: 101Y010: Ankara, Turkey, Report, Scientific and Technical Research Council of Turkey.

NATAL'IN, B. A., SUNAL, G. & TORAMAN, E. 2005. The Strandja arc: anatomy of collision after long-lived arc parallel tectonic transport. In *Structural and Tectonic Correlation across the Central Asia Orogenic Collage: North-Eastern Segment*, (ed. E. V. Sklyarov). Guidebook and abstract volume of the Siberian Workshop, pp. 240–45. IGCP-480, IEC SB RAS, Irkutsk.

OKAY, A. I. & SATIR, M. 2000. Upper Cretaceous eclogite facies metamorphic rocks from the Biga Peninsula, northwest Turkey. *Turkish Journal of Earth Sciences* **9**, 47–56.

OKAY, A. I., SATIR, M., TÜYSÜZ, O., AKYÜZ, S. & CHEN, F. 2001. The tectonics of the Strandja Massif: late-Variscan and mid-Mesozoic deformation and metamorphism in the Northern Aegean. *International Journal of Earth Sciences* **90**, 217–33.

PASSCHIER, C. W. & TROUW, R. A. J. 1996. *Microtectonics*. Berlin: Springer-Verlag, 289 pp.

PERINÇEK, D. 1991. Possible strand of the North Anatolian Fault in the Thrace basin, Turkey – an interpretation. *American Association of Petroleum Geologists, Bulletin* **57**, 241–257.

POUCHOU, J. L. & PICHOIR, F. 1984. A new model for quantitative analyses. I. Application to the analysis of homogeneous samples. *La Recherche Arospatiale* **3**, 13–38.

POUCHOU, J. L. & PICHOIR, F. 1985. 'PAP' (f-r-Z) correction procedure for improved quantitative microanalysis. In *Microbeam Analysis* (ed. J. T. Armstrong), pp. 104–106. San Francisco Press.

PURDY, J. W. & JÄGER, E. 1976. K-Ar ages on rock forming minerals from the Central Alps. *Memoir of the Institute of Geology and Mineralogy, University of Padova* **30**, 1–30.

REDDY, S. M., WHEELER, J., BUTLER, R. W. H., CLIFF, R. A., FREEMAN, S., INGER, S., PICKLES, C. & KELLEY, S. P., 2003. Kinematic reworking and exhumation within the convergent Alpine Orogen. *Tectonophysics* **365**, 77–102.

RICOU, L. E. 1994. Tethys reconstructed: plates, continental fragments and their boundaries since 260 Ma from Central America to South-eastern Asia. *Geodinamica Acta* **7**, 169–218.

SCHUMACHER, J. C. 1997. The estimation of ferric iron in electron microprobe analyses of amphiboles. *European Journal of Mineralogy* **9**, 643–51.

ŞENGÖR, A. M. C., YILMAZ., Y. & SUNGURLU, O. 1984. Tectonics of the Mediterranean Cimmerides: nature and evolution of the western termination of Paleo-Tethys. In *The Geological Evolution of the Eastern Mediterranean* (eds J. E. Dixon & A. H. F. Robinson), pp. 77–112. Geological Society of London, Special Publication no. 17.

SIEBEL, W., REITTER, E., WENZEL, T. & BLAHA, U. 2005. Sr isotope systematics of K-feldspars in plutonic rocks revealed by the Rb–Sr microdrilling technique. *Chemical Geology* **222**, 183–99.

SPEAR, F. S. 1980. NaSi = CaAl exchange equilibrium between plagioclase and amphibole. An empirical model. *Contributions to Mineralogy and Petrology* **72**, 33–41.

SPEAR, F. S. 1981. Amphibole-plagioclase equilibria: an empirical model for the relation albite + tremolite = edenite + 4 quartz. *Contributions to Mineralogy and Petrology* **77**, 355–64.

SPEAR, F. S. 2004. Fast cooling and exhumation of the Valhalla Metamorphic Core Complex, southeastern British Columbia. *International Geology Review* **46**, 193–209.

SPEAR, F. S. & KOHN, M. J. 1999. *Program Thermobarometry (GTB, version 2.1)*. GTB program manual, 42 pp.

STEIGER, R. H. & JÄGER, E. 1977. Subcommission on geochronology: convention on the use of decay constants in geo- and cosmochronology. *Earth and Planetary Science Letters* **36**, 359–62.

SUNAL, G., NATAL'IN, B. A., SATIR, M. & TORAMAN, E. 2006. Paleozoic magmatic events in the Strandja Massif, NW Turkey. *Geodinamica Acta* **19**, 283–300.

SUNAL, G., SATIR, M., NATAL'IN, B. A. & TORAMAN, E. 2008. Paleotectonic position of the Strandja Massif and surrounding continental blocks based on zircon Pb-Pb age studies. *International Geology Review* **50**, 519–45.

TOPUZ, G., ALTHERR, R., SATIR, M. & SCHWARZ, W. H. 2004. Low-grade metamorphic rocks from the Pulur complex, NE Turkey: implications for the pre-Liassic evolution of the Eastern Pontides. *International Journal of Earth Sciences* **93**, 72–91.

TOPUZ, G., OKAY, A. I., ALTHERR, R., SATIR, M. & SCHWARZ, W. H. 2008. Late Cretaceous blueschist-facies metamorphism in the southeastern Thrace (NW Turkey) and its regional implications. *Journal of Metamorphic Geology* **26**, 895–913.

TRICART, P., VAN DER BEEK, P., SCHWARTZ, S. & LABRIN, E. 2007. Diachronous late-stage exhumation across the western Alpine arc: constraints from apatite fission-track thermochronology between the Pelvoux and Dora-Maira Massifs. *Journal of the Geological Society* **164**, 163–74.

TÜRKECAN, A. & YURTSEVER, A. 2002. *Geological map of Turkey; Istanbul*. Ankara, Turkey: Publication of the General Directorate of Mineral Research and Exploration.

VILLA, I. M. 1998. Isotopic closure. *Terra Nova*, **10**, 42–7.
YALTIRAK, C. 2002. Tectonic evolution of the Marmara Sea and its surroundings. *Marine Geology* **190**(1–2), 493–529.
YANEV, S. 2000. Palaeozoic terranes of the Balkan Peninsula in the framework of Pangea assembly. *Palaeogeography, Palaeoclimatology, Palaeoecology* **161**, 151–77.
ZECK, H. P. & HANSEN, B. T. 1988. Rb-Sr mineral ages for the Grenvillian metamorphic development of spilites from the DaMand Supracrustal Group, SW Sweden. *Geologische Rundschau* **77/3**, 638−92.

https://doi.org/10.1017/S0016756810001020 Published online by Cambridge University Press